Journal of Computational Physics **172,** 515–542 (2001)
doi:10.1006/jcph.2001.6835, available online at http://www.idealibrary.com on

A Vorticity-Based Method for Incompressible Unsteady Viscous Flows

L. Qian and M. Vezza

Department of Aerospace Engineering, University of Glasgow, Glasgow G12 8QQ, Scotland, United Kingdom

Received May 30, 2000; revised April 6, 2001

A novel approach is presented, based on the integral form of the vorticity formulation, in which the vorticity transport equation is solved by using the cell-centred finite-volume method, while the velocities needed at the centre of each control volume are calculated by a modified Biot–Savart formula in conjunction with a fast summation algorithm. The vorticity and mass conservation in the flow are guaranteed during the calculation by virtue of the finite volume approach and the method of implementing the boundary conditions at the body surface. As an example, both the early stage development and long term evolution of the flow around an impulsively started circular cylinder are computed using the method. The present results are compared with other numerical and experimental results for the same flow problem and show good agreement.

---

1. INTRODUCTION

Vorticity and its related quantities, such as circulation, played an important role in classic theoretical fluid dynamics [2, 18]. More recently, with the advent and rapid development of computer technology, vorticity-based methods have become one of the main focus areas of research in computational fluid dynamics. These methods can be generally divided into two categories, in terms of the governing equations upon which the numerical formulations are constructed. One is based on the differential form of the Navier–Stokes equations, either in the velocity–vorticity or velocity–vector potential (stream function for 2-D cases) formulations. The other is the so-called differential-integral formulation [36], in which an integral equation for calculating velocity explicitly from the vorticity field is employed in place of the continuity equation and the definition of vorticity, while the vorticity transport equation remains in the differential form. This latter formulation is interesting in that, first, it separates the kinematics (velocity calculation) from the kinetics (vorticity redistribution), which allows explicit, point-by-point calculation of velocity, and the velocity boundary condition at infinity is exactly satisfied. Secondly, in this formulation, only the (usually compact) fluid region with non-zero vorticity needs to be solved.

0021-9991/01 $35.00

During the past two decades, by using the differential–integral formulation, both the grid-based Euler method and the gridless Lagrangian method have been used to advance the solution in the space–time domain. The latter is usually referred to as the discrete vortex method, which has become more popular in recent years. In the pioneering works of Wu and coworkers, a finite difference scheme was used to solve the vorticity transport equation in the transformed complex plane. The integral equation for the velocity was solved by using finite Fourier series expansions of the field variables at each circular ring of the O-grid and partially evaluated analytically [33, 35]. Meanwhile, to reduce the possibility of numerical diffusion in the grid-based method, the Lagrangian discrete vortex method has been developed and applied, notably by Chorin [8], Leonard [21, 22], Sarpkaya [28], and more recently among others by Spalart [32], Koumoutsakos and Leonard [19], and Lin *et al.* [24]. In this method, the continuous vorticity field is represented by a number of overlapping vortex particles which are tracked in the flow according to the local velocity calculated by the Biot–Savart law. To combat the associated high computational cost of the velocity calculation, adaptive fast summation algorithms have been developed [12, 15, 16], which reduce the operational cost from $O(N^2)$ to $O(N \log N)$ depending on the implementation details, where N is the total number of vortices in the flow. This method has been applied to calculate a number of unsteady flow problems, such as bluff body flow [19] and the flow around a pitching aerofoil under the condition of dynamic stall [24, 32]. Problems, however, with the discrete vortex method are that, first, after some period of evolution of the vortices, the particle distribution may become uneven, thus destroying the overlapping condition which necessitates a remeshing process [19]. In addition, a large number of vortices are needed to capture the fine flow structures near the surface of the body. Secondly, it is not straightforward to include viscous effects, including turbulence, in the calculation, although some developments have been made recently [29]. Lastly, it is not clear how best to extend the method to 3-D flow problems, due to the fact, among others, that the vortex particle representation in 3-D is not divergence-free.

In this paper, a novel approach has been adopted for solving the differential–integral form of the Navier–Stokes equations—namely, the cell-centred finite-volume method has been applied to the integral form of the vorticity transport equation, while the velocities needed at the centre of each control volume are calculated by using a modified Biot–Savart formula in conjunction with an adaptive fast summation algorithm. The methods employed to implement the boundary conditions and to calculate the vorticity creation at the body surface ensure that both the mass and vorticity are conserved during the calculation. This, along with the inherent conservative property of the finite-volume method, guarantees the conservation of vorticity in the entire flow. Because the same strategy as the discrete vortex method has been used to calculate the velocity, the present method can be easily coupled with the discrete vortex method in the domain decomposition approach [9, 31]; i.e., the present method can be used in the viscous region near the body surface and the vortex particle method can be applied to the outer region of the essentially inviscid flow. Furthermore, it is straightforward to extend the method to 3-D flow problems, although the question of vorticity divergence remains.

In the following sections, the theoretical background of the method is reviewed, followed by a detailed description of the numerical implementation, including the fast summation algorithm and implementation of boundary conditions. By calculating the unsteady flow around a circular cylinder at various Reynolds numbers, the accuracy and efficiency of the method are demonstrated and the effect of different implementations of boundary conditions on the solution is analysed. Finally, some conclusions are drawn from the study and a brief discussion of future work is given.

2. MATHEMATICAL FORMULATION

Two-dimensional incompressible viscous flow can be described by the vorticity (ω)–velocity ($\vec{u}$) form of the Navier–Stokes equations[36], which include

vorticity transport equation

$$\frac{d\omega}{dt} = \frac{\partial \omega}{\partial t} + \vec{u} \cdot \nabla \omega = \nu \nabla^2 \omega \tag{1}$$

continuity equation

$$\nabla \cdot \vec{u} = 0 \tag{2}$$

the definition of vorticity

$$\omega = \frac{\partial v}{\partial x} - \frac{\partial u}{\partial y} \ . \tag{3}$$

For the problem of flow around a closed body, the boundary conditions needed for solving the governing equations consist of two parts, both of which are given in terms of velocity. One is the so-called, far field condition in which the free-stream condition is applied at infinity:

$$\vec{u} = \vec{u}_\infty . \tag{4}$$

The other is the condition on the body surface where the no-slip and no-penetration conditions are imposed

$$\vec{u} = \vec{u}_b(\vec{x}_s, t), \tag{5}$$

where $\vec{u}_b(\vec{x}_s, t)$ represents the velocity at the body surface. For the present formulation, however, only one of the no-slip and no-penetration conditions is needed to uniquely determine the velocity field from the vorticity distribution using Eqs. (2) and (3), which in turn determines the vorticity boundary condition needed for solving the vorticity transport equation. Theoretically, in this aspect, it can be shown that [2, 23, 36], the no-slip boundary condition and no-penetration condition are equivalent in determining the vorticity boundary condition; i.e., implementation of no-slip condition leads to satisfying the no-penetration condition, and vice versa.

For unsteady flow problems, initial conditions are also required to start the calculation. This is achieved by either assuming that the flow starts impulsively from rest or prescribing the velocity or vorticity distribution in the flow field.

It has long been known from the Helmholtz theory that the velocity field can be uniquely determined from the vorticity field and relevant velocity boundary conditions. Quantitatively, an explicit relationship between the velocity field and vorticity field has been given by Wu and Thompson [36] through solving Eqs. (2) and (3) using Green's identity and the boundary conditions given in Eqs. (4) and (5),

$$\vec{u}(\vec{x},t)=\frac{1}{2\pi}\int_D\frac{\omega(\vec{x}',t)\vec{k}\times(\vec{x}-\vec{x}')}{|\vec{x}-\vec{x}'|^2}dA+\vec{u}_\infty, \tag{6}$$

where the integral over area D in Eq. (6) is taken over the portion of the region containing non-zero vorticity in fluid and rotating solid body. Equation (6) is a particular application of the Biot–Savart law. The use of Eq. (6) to calculate velocity from the integral over vorticity also makes it possible that only the non-zero vorticity region needs to be solved, which differs from most other vorticity-based methods in differential form of the governing equations. Another issue in the vorticity-based formulation is the conservation of vorticity. From this condition for a stationary body, it can be stated that the entire vorticity entering the fluid region through the body surface(see Fig. 1) should always be zero,

$$\oint_{bs}\nu\frac{\partial\omega}{\partial n'}\,ds'=0. \tag{7}$$

The importance of this condition in constructing a numerical method will be discussed in detail later.

It is well known that for incompressible viscous flow, the vorticity can only be generated at the surface of the body due to the no-slip boundary condition. The vorticity in the interior of the fluid domain, which in turn determines the velocity field through the Biot–Savart law, is the consequence of diffusion and convection of the boundary vorticity. From this basic idea, together with Eqs. (1) and (6) which represent the kinetic and kinematic aspects of the entire flow problem, respectively, vorticity-based methods [8, 36], including the present method, can be constructed. The kinematic step determines the velocity field induced by the vorticity distribution and relevant boundary conditions, while the kinetic step redistributes the vorticity within the flow domain by convection and diffusion. In the real world, these two steps should occur simultaneously; however, in the numerical procedure, it is reasonable

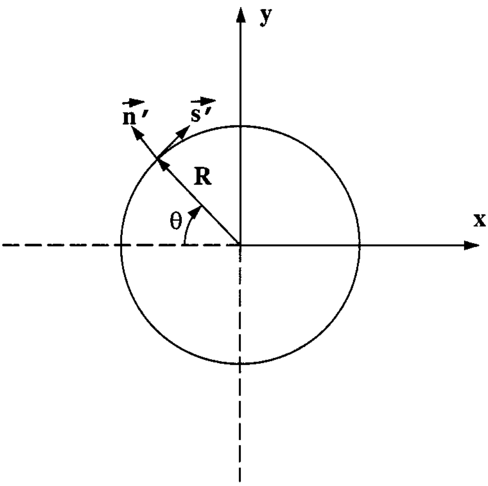

FIG. 1. Definition sketch of the flow around a cylinder.

to assume that the following three steps are needed to advance the solution to a new time level:

1. calculation of vorticity creation in terms of vorticity flux into the flow through the surface (boundary vorticity) by using Eq. (6) and implementing the relevant boundary conditions—this process usually leads to a system of linear algebraic equations to be solved at every time step with vorticity flux or boundary vorticity values as the unknowns;
2. calculation of the velocity using the Biot–Savart Law; note that, at this step, the vorticity in Eq. (6) includes the newly created vorticity from the body surface through viscous diffusion (flux).
3. redistribution of the vorticity in the flow field by solving the vorticity transport equation.

After step 3, the velocity boundary condition at the body surface is usually no longer satisfied and we need to return to step 1, which constitutes a full loop.

The following sections will detail the specific methods used in the current study for each part of the three steps.

3. NUMERICAL IMPLEMENTATION

3.1. *Solution of Vorticity Transport Equation*

The solution of the vorticity transport equation using the cell-centred finite volume method is straightforward. For each control volume Ω_c, see Fig. 2, the vorticity transport equation can be written in the integral form

$$\frac{\partial}{\partial t}\int_{\Omega_c}\omega\, d\Omega + \int_s \vec{u}\omega\cdot\vec{n}\, ds = \nu\int_s \nabla\omega\cdot\vec{n}\, ds, \tag{8}$$

where $\vec{n}$ is the unit normal vector of the control volume surface s.

In the present study, the two-stage, second-order Runge–Kutta method has been used to advance the solution in the time domain and either the second-order central scheme (middle point rule) or the upwind scheme, depending on the local grid Reynolds number, is used to calculate the convective flux term for each of the cell faces. For diffusive fluxes, a simple linear interpolation can be used for calculating the gradient for an orthogonal coordinate system which is the case in the present study. If more general cases with non-orthogonal

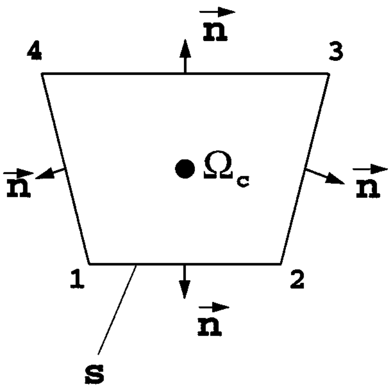

FIG. 2. Control volume.

coordinate systems are involved, the method involving the transformation of the derivative into a surface integral using the Gauss theorem can be employed [13].

Since the vorticity transport equation, which redistributes the vorticity within the fluid domain, is solved in the conservative form by using the finite volume approach, no vorticity will be generated in this process by numerical errors and the only concern of vorticity conservation will lie entirely on the process of vorticity generation at the solid boundaries, which will be discussed later.

3.2. *Velocity Calculation*

Once the vorticity distribution in the flow is known, the velocities needed at the centres of the control volumes with non-zero vorticity and some neighbouring control volumes with zero vorticity can be calculated by using Eq. (6). By assuming the vorticity has a uniform distribution within each control volume when evaluating the integral in Eq. (6), which is consistent with the cell-centred finite-volume approach, the velocity at a point $\vec{x}_j$, in particular at the centre of each control volume, is given by

$$\vec{u}_j(\vec{x}_j, t) = \frac{1}{2\pi} \sum_{i=1}^{N_v} \int_{\Omega_i} \frac{\omega_i(t)\vec{k} \times (\vec{x}_j - \vec{x}')}{|\vec{x}_j - \vec{x}|^2}\, d\Omega_i + \vec{u}_\infty, \tag{9}$$

where N_v is the total number of the control volumes on which the integral is performed.

For each control volume Ω_i, by virtue of the following vector identities, $\nabla \times (f\vec{G}) = f\nabla \times \vec{G} + \nabla f \times \vec{G}$ and $\int\int \nabla \times \vec{G}\ \ d\Omega = \int \vec{G} \times \vec{n}\ ds$, the integral in Eq. (9) can be transformed into the circuit integral around the cell, see Fig. 3,

$$\int_{\Omega_i} \frac{\omega_i(t)\vec{k} \times (\vec{x}_j - \vec{x}')}{|\vec{x}_j - \vec{x}'|^2}\, d\Omega_i \tag{10}$$

$$= -\int_{\Omega i} \omega_i(t)\vec{k} \times \nabla' \ln|\vec{x}_j - \vec{x}'|\, d\Omega_i \tag{11}$$

$$= \int_{\Omega_i} \nabla' \times (\omega_i(t)\vec{k} \ln|\vec{x}_j - \vec{x}'|\, d\Omega_i \tag{12}$$

$$= \int_{S_i} \omega_i(t)\vec{k} \times \vec{n} \ln|\vec{x}_j - \vec{x}'|\, ds \tag{13}$$

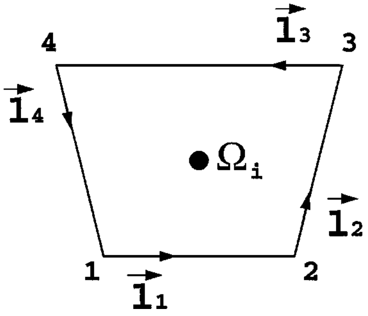

FIG. 3. Velocity contribution from each control volume.

$$= \omega_i(t) \sum_{k=1}^{4} \vec{l}_k \int_{lk} \ln |\vec{x}_j - \vec{x}'| \, dl_k \tag{14}$$

$$= \omega_i(t) \vec{S}_i, \tag{15}$$

where $\vec{l}_k$ is the unit direction vector of the cell segment l_k and quadrilateral cells have been assumed. To evaluate the integral, either an analytic expression or numerical approximation can be used, and for the neighbouring cells, the integral needs to be calculated only once for their common segment.

It is easy to check that in calculating the velocity at a point (cell centre), the influence of all the cells with non-zero vorticity must be taken into account. This involves a calculation of $O(N_v^2)$ interactions for N_v control volumes with non-zero vorticity, which can lead to a large computational cost.

Fortunately, during the past decade, several fast summation algorithms have been developed originally for the discrete vortex method. In this study, the adaptive fast algorithm proposed by Van Dommelen *et al.* [12] has been modified for calculating the velocity field. The basic idea in the method is that when the velocity at the centre, $\vec{x}_i$ say, of a control volume Ω_i of area A_{Ω_i} is calculated, the influence of vorticity from the entire flow domain can be divided into the near field, on which the direct summation using Eq. (15) will be performed, and far field, in which a point vortex with strength $\Gamma_i = \omega_i A_{\Omega_i}$ located at $\vec{x}_i$ is used temporarily to represent the entire vorticity in the control volume Ω_i and the indirect fast summation method can be applied

$$\vec{u}(\vec{x}_i) = \tilde{u}'(\vec{x}_i)|_{near\ field} + \tilde{u}^{\tau}(\vec{x}_i)|_{far\ field} \tag{16}$$

in which we have

$$\tilde{u}'(\vec{x}_i)|_{near\ field} = \frac{1}{2\pi} \sum_{j=1}^{N_D} \omega_j(t) \sum_{k=1}^{4} \vec{l}_k \int_{l_k} \ln |\vec{x}_j - \vec{x}_i| \, dl_k \tag{17}$$

and

$$\tilde{u}^{\tau}(\vec{x}_i)|_{far\ field} = \frac{1}{2\pi} \sum_{j=1}^{N_F} \Gamma_j \vec{k} \times \frac{\vec{x}_i - \vec{x}_j}{|\vec{x}_i - \vec{x}_j|^2}, \tag{18}$$

where N_D and N_F are the total number of control volumes which are eligible for direct summation and indirect (fast) summation, respectively.

By using the complex notation, Eq. (18) can be expressed as

$$u^{\tau}(Z_i) - i v^{\tau}(Z_i) = \frac{1}{2\pi i} \sum_{j=1}^{N_F} \frac{1}{Z_i - Z_j}, \tag{19}$$

where Z is the complex position of $\vec{x}$ and u^{τ} and v^{τ} are the two components of $\tilde{u}^{\tau}$.

The only criterion for calculating the near field or far field effects can be determined by the following process. To implement the fast summation algorithm efficiently, a square adaptive zonal decomposition is employed. The whole flow domain containing non-zero

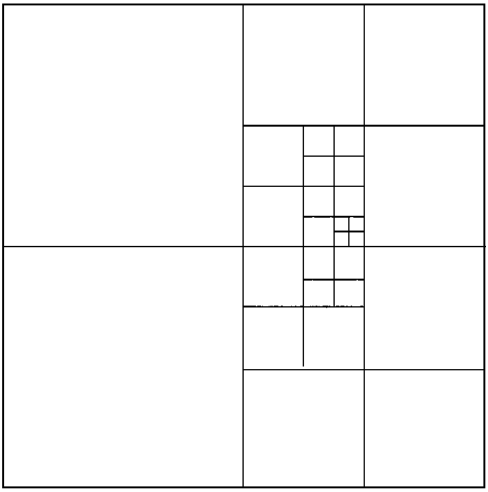

FIG. 4. Adaptive fast summation algorithm.

vorticity is initially contained in a single square zone. This is then divided into four sub-zones. Each zone is then further subdivided into four new zones, provided that there is a minimun number of particles in the zone, thus creating a hierarchical structure of zones as shown in Fig. 4. For each zone, the parent zone and any children (sub-zones) of the zone are recorded, along with which particles are stored in that zone. By using the complex notation, the centres of the control volume i and the zone can be represented by Z_i and Z_c, respectively. Then the contribution of the zone to the velocity at point Z_i can be calculated from a series expansion using Eq. (20) below, provided the distance between Z_i and Z_c is greater than some factor times the radius λ of the zone so that the Laurent series will converge

$$u^\tau(Z_i) - i v^\tau(Z_i) = \sum_{k=1}^{N_t} \frac{\alpha_k}{2\pi i (Z_i - Z_c)^k}, \tag{20}$$

where $\alpha_k = \sum_j^{N_p} \Gamma_j (Z_i - Z_c)^{k-1}$ and N_p is the total number of vortex particles contained in the zone. Once the influence of a zone is calculated, the children of this zone are then ignored, as all the particles in the zone have been taken into account. If the centre of a control volume is too close to Z_c for the series to converge, then the zone's children are considered in the same way. This process continues until the series expansion can be used, or the smallest zone is reached, and if the series will still not converge, the velocity contribution is calculated from direct summation. The hierarchical structure in the algorithm means that the largest possible zone is used at all times.

3.3. *Implementation of Boundary Conditions*

For convenience of description, in the following sections the cells immediately adjacent to the body surface will be referred to as boundary cells and the remaining cells are called non-boundary cells. At each time step t, after solving the vorticity transport equation, the new vorticity values at time $t + \Delta t$ in the non-boundary cells are known. For the boundary cells, however, the new vorticity values depend not only on the neighbouring cells through

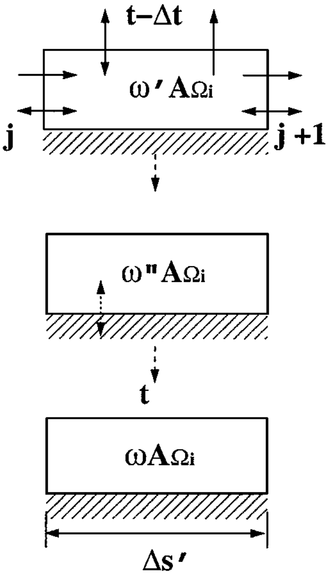

FIG. 5. Surface vorticity flux calculation.

convection and diffusion, but also on the new vorticity (flux) created at the body surface during the time step Δt. The rate of the vorticity creation per unit length at the body surface can be represented by $-\nu\frac{\partial\omega}{\partial n'}$. Considering a boundary control volume with node points j and $j+1$ shown in Fig. 5, the vorticity at time $t-\Delta t$ is assumed to be ω'. After convection and diffusion through the interfaces (not including the new vorticity generated at the body surface) during a time interval Δt, which is represented by the symbols $\rightarrow$ and $\leftrightarrow$, respectively, the residual vorticity will be ω''. If the new vorticity in the control volume at time t is calculated as ω, then the vorticity flux per unit length through the body surface is

$$-\nu\frac{\partial\omega}{\partial n'} = \frac{(\omega-\omega'')A_{\Omega_i}}{\Delta t\,\Delta s'}, \tag{21}$$

where A_{Ω_i} is the area of control volume Ω_i.

The new vorticity values for each boundary control volume, and hence the surface vorticity flux entering each boundary control volume, can then be determined by implementing the velocity boundary conditions. This leads to a set of linear algebraic equations which must be solved at each time step to obtain the vorticty in the boundary cells.

Theoretically, for the formulation based on the vorticity and velocity description of the flow, the no-penetration and no-slip conditions are equivalent in determining the boundary vorticity flux; that is, either condition can be used but not both [23, 36]. More specifically, if the no-slip condition is used, the no-penetration condition will be automatically satisfied, and vice versa. In such a way, the entire boundary condition stated in Eq. (5) can be satisfied without overspecifying the problem. In the actual calculation, the contour of the body is divided into a number of panels, each of which also constitutes a segment (face) of the boundary cells. If the no-slip condition is implemented, then, for each panel, a control point must be chosen on which the tangential velocity induced by all the cells is zero. Usually, the midpoint or quarter point of the panel is used. However, although it can be proven that implementation of the no-slip boundary condition leads to conservation of vorticity in the flow field, it is impossible, by the numerical approach, to enforce the zero tangential velocity condition at all points along the panel, which, it has been found, can lead to large errors for long time calculation, as vorticity conservation cannot be guaranteed. One alternative approach to satisfying the boundary conditions is by using the no-penetration condition, which can, of course, be implemented at only one point for each panel. The best way, which is implemented in the present study, is to ensure the mass flux through each panel is zero by using $\int_{P_j} \vec{u} \cdot \vec{n}' ds' = 0$, if the body is stationary, for panel P_j with node points j and $j+1$. More specifically, for each panel P_j, $j = 1, 2, \ldots, N_p$, the mass flux F_j' due to the velocity field in the flow region consists of three parts; that is,

$$F_j' = \int_{P_j} \vec{u} \cdot \vec{n}' ds' = F_{jF} + F_{jB} + F_{jW}, \tag{22}$$

which represents respectively the contribution from the free stream, vorticity in the boundary cells and vorticity in the remaining cells. The flux from the free stream F_{jF} can be calculated as

$$F_{jF} = \int_j \vec{u}_\infty \cdot \vec{n}' ds_j' \tag{23}$$

while the flux from the vorticity in the boundary cells is

$$F_{jB} = \sum_{i=1}^{N_p} \omega_i(t) \int_j (\vec{S}_i \cdot \vec{n}')\, ds_j', \tag{24}$$

where vorticity values $\omega_i(t)$, $i = 1, 2 \ldots N_p$ are unknowns to be solved at each time step and meaning of the vector $\vec{S}_i$ can be found in Eq. (14) and (15). The flux from the remaining cells with non-zero vorticity is

$$F_{jW} = \sum_{i=1}^{N_w} \omega_i(t) \int_j (\vec{S}_i \cdot \vec{n}')\, ds_j', \tag{25}$$

where N_w is the total number of those cells. Note that, in Eq. (24), the vorticity in each boundary cell includes the newly created vorticity from the body surface during the time step from $t - \Delta t$ to t and the relationship between this vorticity and the vorticity flux from the body surface is given by Eq. (21).

On the other hand, it can be shown that if the no-penetration boundary condition is implemented for $N_p - 1$ panels, then this condition will be automatically satisfied for the remaining panel. In other words, for N_p panels, only $N_p - 1$ equations are independent and another equation is needed to make the solution unique. Fortunately, the requirement of vorticity conservation, or more specifically, the integral of the vorticity flux at the body surface being zero for a stationary body, can be used as the supplemental equation:

$$\sum_{j=1}^{N_p} \int_j -\nu \frac{\partial \omega}{\partial n'}\, ds_j' = 0. \tag{26}$$

The advantage of this approach is that the conservation of both mass and vorticity in the entire flow can be guaranteed during the calculation.

3.4. *Calculation of Surface Pressure and Body Forces*

For viscous flow, the forces exerted on the body come from two sources: surface pressure distribution and surface friction. For the body-oriented local orthogonal coordinate system $(\vec{s}', \vec{n}')$, the tangential momentum equation can be written at the surface of a stationary body as

$$\frac{1}{\rho}\frac{\partial p}{\partial s'} = -\nu \vec{s}' \cdot (\nabla \times \vec{\omega}), \tag{27}$$

which can be reduced to

$$\frac{1}{\rho}\frac{\partial p}{\partial s'} = -\nu \frac{\partial \omega}{\partial n'} . \tag{28}$$

The term on the right-hand side of the equation is the rate of vorticity creation per unit length at the solid surface and is known for each panel after implementing the boundary conditions. So for each panel at the surface, the pressure gradient can be calculated as

$$\frac{p_j - p_{j-1}}{\rho \Delta s'_j} = -\nu \frac{\partial \omega}{\partial n'} . \tag{29}$$

Once the pressure value at a reference point is assumed, the entire pressure distribution along the body surface can be easily calculated by integrating Eq. (29) and the body forces exerted by the surrounding fluid can then be integrated from the surface pressure distribution and the tangential friction force.

For the particular case of flow around a circular cylinder, the drag and lift can be obtained from

$$L = R \oint_{bs} \left(\mu R \frac{\partial \omega}{\partial n'} - \mu \omega \right) \cos\theta \, d\theta \tag{30}$$

$$D = R \oint_{bs} \left(\mu R \frac{\partial \omega}{\partial n'} - \mu \omega \right) \sin\theta \, d\theta \tag{31}$$

and the non-dimensional drag and lift coefficients of the body are then given by

$$C_D = \frac{D}{\rho U_\infty^2 R} \tag{32}$$

and

$$C_L = \frac{D}{\rho U_\infty^2 R}, \tag{33}$$

where R is the radius of the circular cylinder.

4. RESULTS AND DISCUSSION

To show the accuracy and efficiency of the proposed method, a number of calculations have been carried out for the flow around an impulsively started circular cylinder. This flow

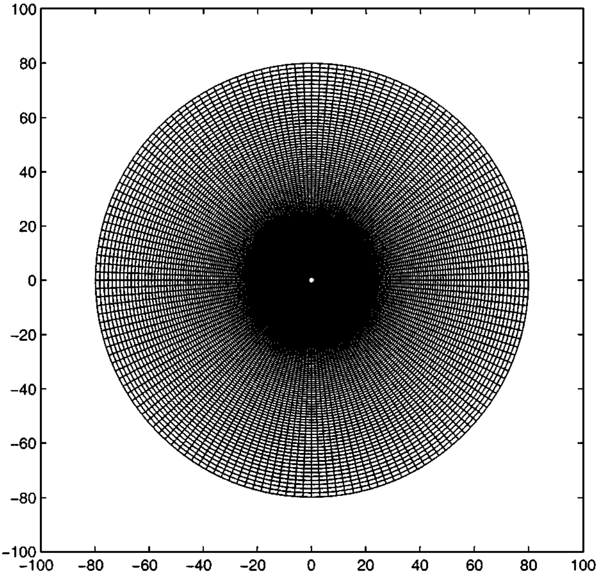

FIG. 6. Coordinate system and the grids.

problem has been extensively used as a prototype of unsteady separated flows and a number of numerical and experimental results are available for validating new numerical methods. In Fig. 6, the simple polar coordinate system used for the calculation is shown, in which the grid is uniformly distributed in the θ direction and is stretched exponentially in the r direction. Since the grids (cells) are needed only for the non-zero vorticity region, a small portion of the entire grids are used in the actual calculation. In the following discussions, both early stage development of the flow at various Reynolds numbers ($Re = 2U_\infty R/\nu$) and long time evolution of the wake (Karman vortex street) for $Re = 1000$ are presented, and where possible, comparisons are made with other numerical and experimental results, particularly with the results of the high resolution simulations using the discrete vortex methods [19, 29]. In [29], their results have been compared with a number of theoretical, numerical, and experimental results, which provide a useful and reliable database for validating the present method.

4.1. *Fast Algorithm vs Direct Summation*

To examine the performance (timing, accuracy, etc.) of the fast summation algorithm, calculations using both the direct summation and fast algorithm are performed for a Reynolds number of 1000. The grid points used are 160×80 and the size of the first grid cell in the normal direction to the surface is $\Delta Y_1 = 0.02$. The time step adopted for the calculation is $\Delta t = 0.01$ and 600 time steps have been advanced. By the last time step ($T = 6$), the number of active cells, i.e., the cells with a vorticity value not less than a specified value $\epsilon = 10^{-6}$, is about 5600 and the CPU time used for the direct calculation is nearly six times that of the fast algorithm. The number of terms used for calculating the Laurent series expansion is $N_t = 12$. In Fig. 7, the drag coefficients from both calculations are given and no noticeable discrepancy occurs, which indicates the high accuracy of the fast algorithm. The vorticity contours at $T = 5$ and $T = 6$ from the fast algorithm are also compared in

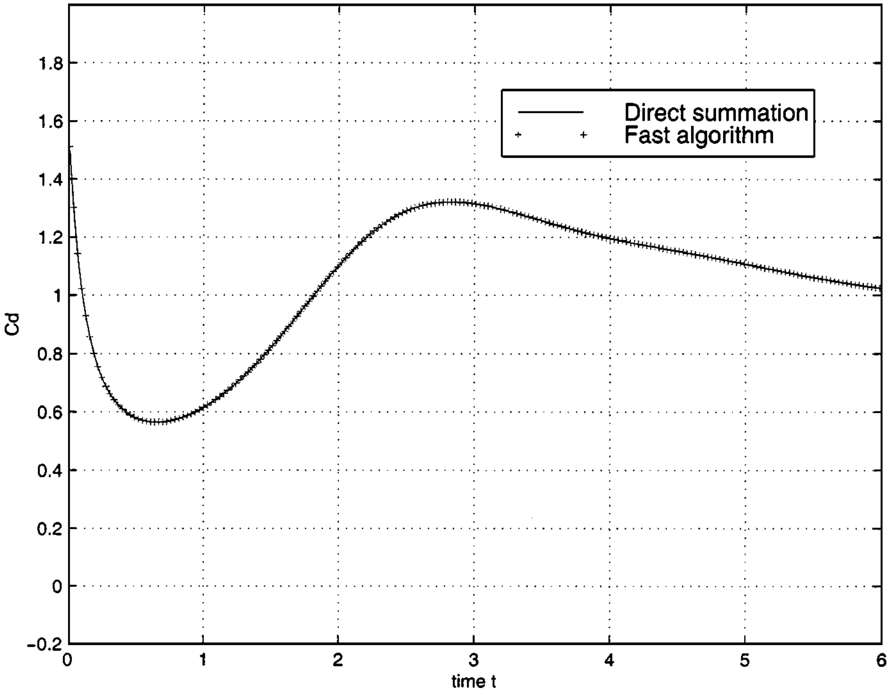

FIG. 7. Accuracy of the fast algorithm: Drag coefficient.

Fig. 8 with its counterpart from the direct summation and, again, the two results are nearly identical. During the calculation, no attempt has been made regarding the optimisation of the fast algorithm and in the future, this will be investigated to gain the maximum benefit in this regard. In the following discussion, all the results are obtained by using the fast summation algorithm for calculating the velocity field.

4.2. *Grid Effects*

In order to evaluate the influence of the grid density on the solution, two cases have been calculated for different grid sizes at *Re* = 1000. For the coarser grid, we have grid nodes $I \times J = 160 \times 80$ and $\Delta\theta = 2\pi/160$, $\Delta Y_1 = 0.02$; and when the grid nodes increase to 320×160, the size of the grids has been halved in both directions. In Fig. 9, the drag coefficients calculated from the different grids are compared. The very small discrepancy indicates the grid systems are fine enough to capture all the flow structures for the Reynolds number considered. In Fig. 10, the streamline patterns at $T = 5$ are also shown for the two cases, from which it can be seen that, although a slight difference in the size of the secondary vortex is noticeable, the global structures of the flow are the same.

4.3. *Comparison with Other Results*

In this section, a number of comparisons are made between the present results and other numerical and experimental results for four different Reynolds numbers: *Re* = 550, 1000, 3000, and 9500, which represents the typical cases in terms of validation of numerical codes [19].

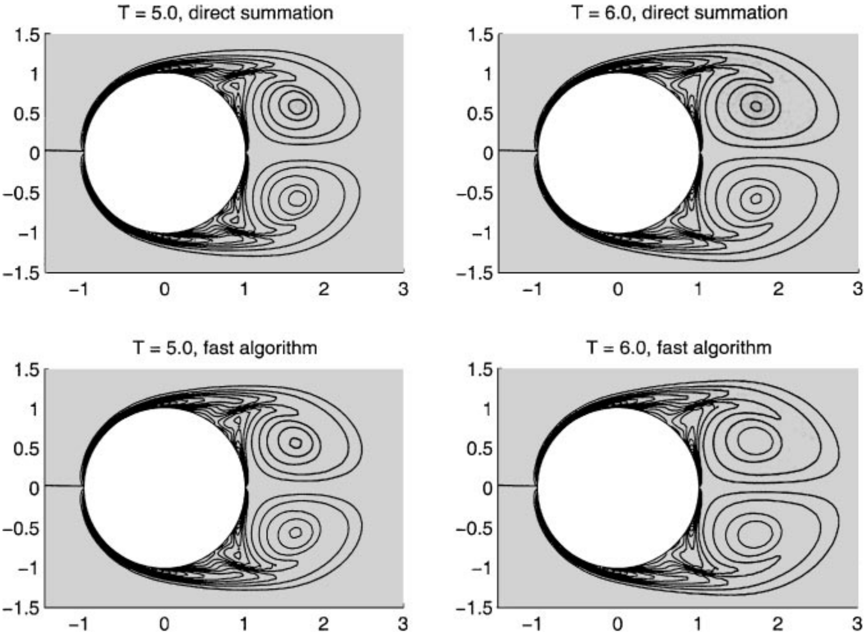

FIG. 8. Accuracy of the fast algorithm: Vorticity contours.

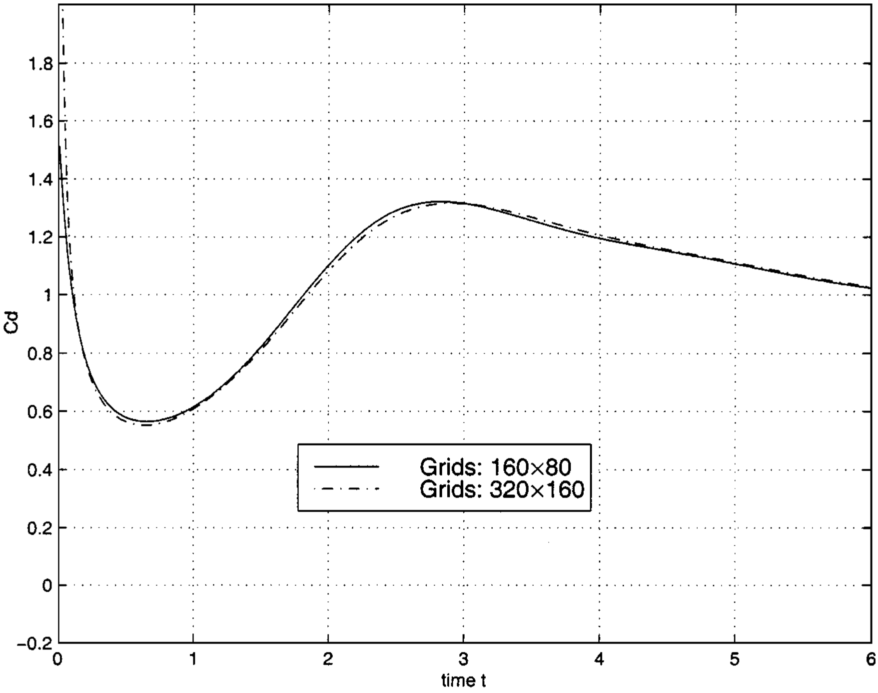

FIG. 9. Effect of grid density on the drag coefficient.

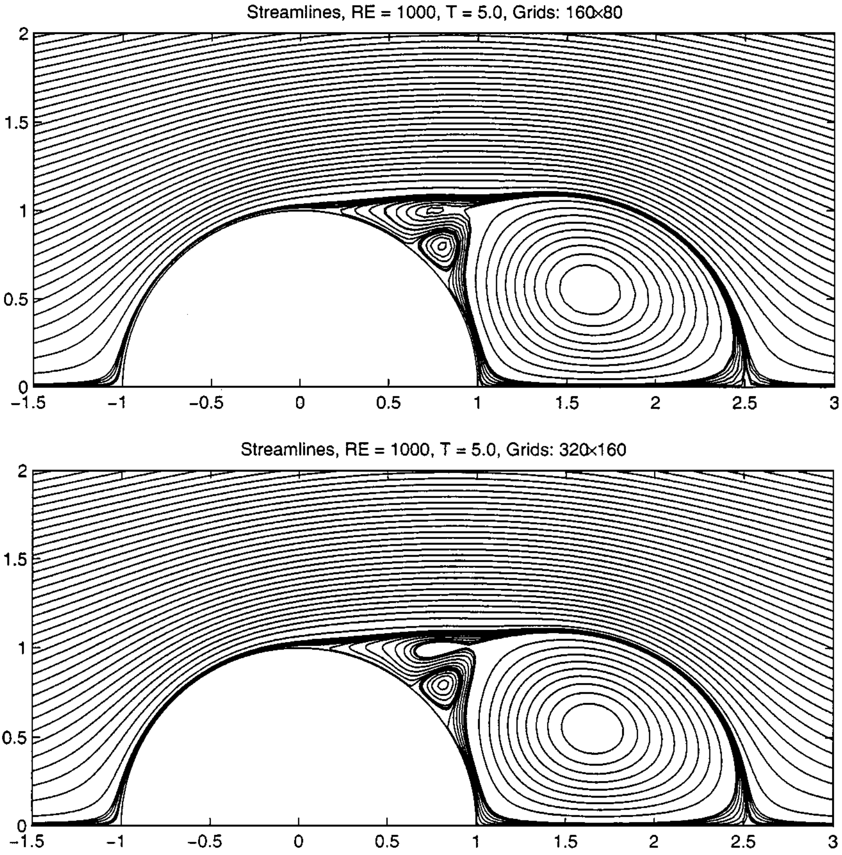

FIG. 10. Effect of grid density on the streamlines.

Re $=$ *550.* In this test case, 160×80 total grid points have been used with a minimum grid size in the normal direction to the surface $\Delta Y_1 = 0.02$ and the time step $\Delta t = 0.01$. In Fig. 11, the drag coefficient C_d for $T < 5.0$ is plotted and compared with the result from Shankar and Van Dommelen [29], which shows a very good agreement. In Fig. 12, the radial velocity distributions along the rear centre line of the circular cylinder are also compared with the result from [29] for $T = 1.0, 2.0, 3.0, 4.0$, and 5.0, and again excellent agreement has been achieved.

Re $=$ *1000.* For this case, 160×80 grid points have been used and the time step to advance the solution is $\Delta t = 0.01$. In Fig. 13, the history of vorticity development for the impulsively started flow are illustrated by the equi-vorticity contours, which shows that, after the sudden start of the flow, the primary vortex is formed at the rear of the cylinder and then, after time reaches $T = 2$, a secondary vortex begins to form and grow in the middle of the main vortex. The corresponding streamline pattern for $T = 5$ is given in Fig. 10, which clearly shows the secondary vortex is interacting with the primary vortex forming the so-called α phenomenon. The vorticity distribution at the surface for several instants of time are given in Fig. 14. Generally, the present results are in good agreement with those from the computations of Koumoutsakos and Leonard using a high resolution discrete vortex method [19].

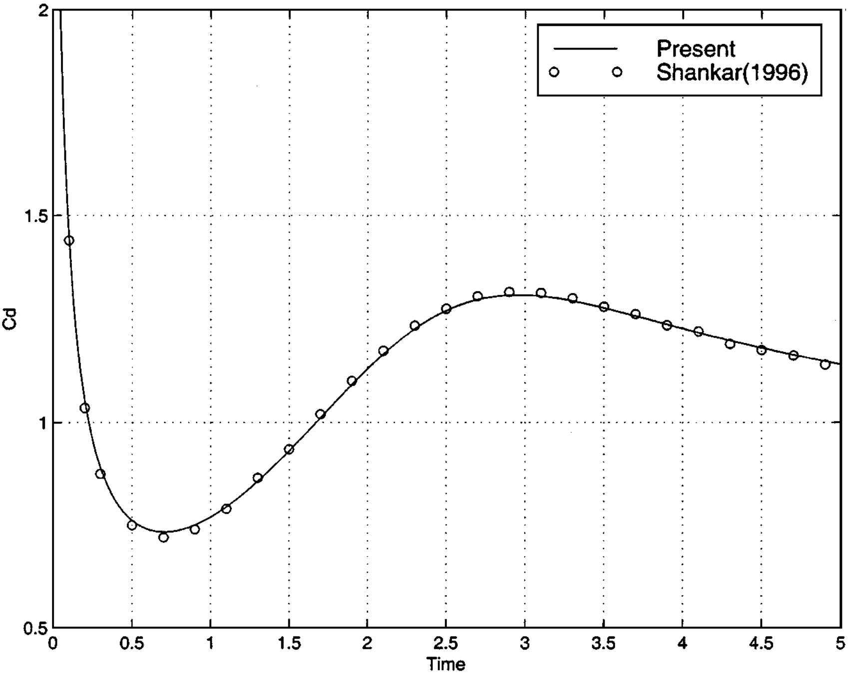

FIG. 11. Comparison of drag coefficients, $Re = 550$.

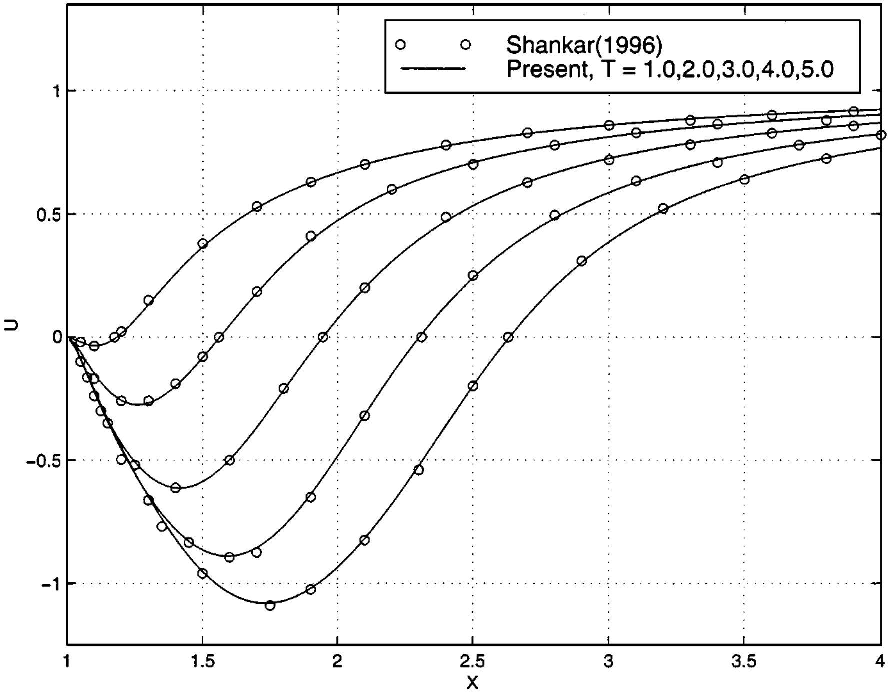

FIG. 12. Radial velocity distribution along the rear centre line of the circular cylinder, $Re = 550$.

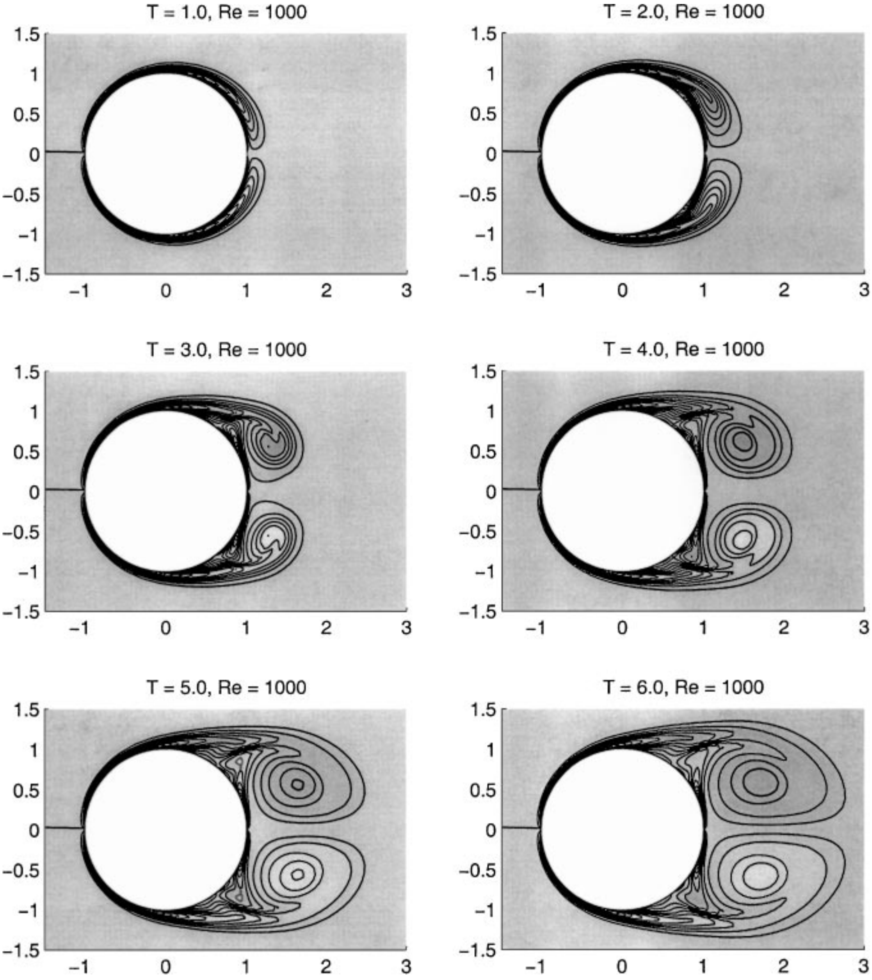

FIG. 13. Vorticity contours: $Re = 1000$.

Figure 15 compares the drag coefficient evolution from the present study with other numerical results. From this figure, it can be seen that the present result agrees particularly well with the result from [19], although at least an order of magnitude more vortex elements were reportedly used for their simulation.

$Re = 3000$. As discussed by Koumoutsakos and Leonard [19], at this Reynolds number, a series of new separation phenomena appear, which poses a challenge for numerical methods to capture all the flow structures. For the results presented, 240×150 grid points have been used with a minimum grid size in the normal direction to the surface $\Delta Y_1 = 0.01$ and the time step $\Delta t = 0.005$. Figs. 16 and 17 show the vorticity distribution at the body surface and the equi-vorticity contours for $T = 1.0, 2.0, 3.0, 4.0, 5.0$, and 6.0, respectively. The interplay between the main vorticity and the secondary vorticity during the flow evolution has been explained in [19] and is reflected in the development of the drag coefficient. For this particular case, a drag plateau

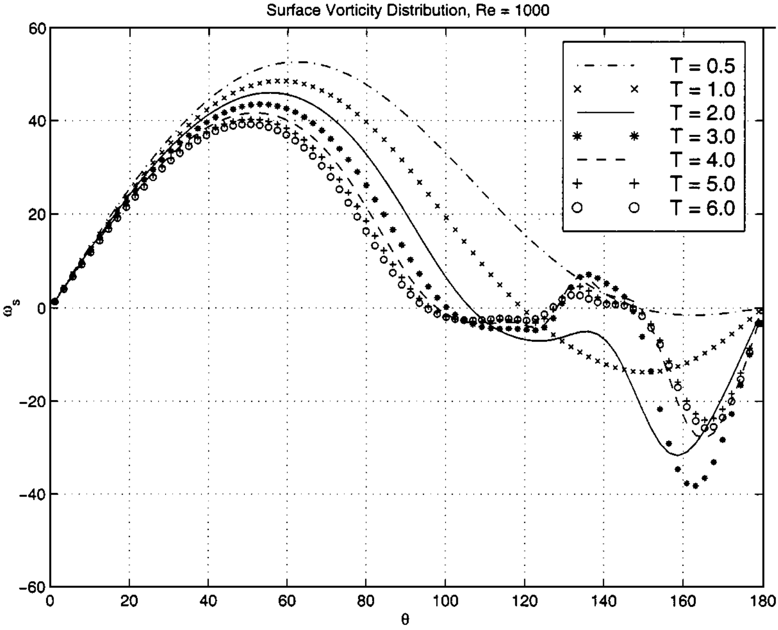

FIG. 14. Surface vorticity distribution: $Re = 1000$.

appears between $T = 2.2$ and $T = 3.0$. From Fig. 18, it can been seen that this phenomenon has been captured by the present method and the results compare well with those presented by Koumoutsakos and Leonard [19] and Shankar and Van Dommelen [29]. For the present study, by the end of the calculation ($T = 6.0$), the number of active cells

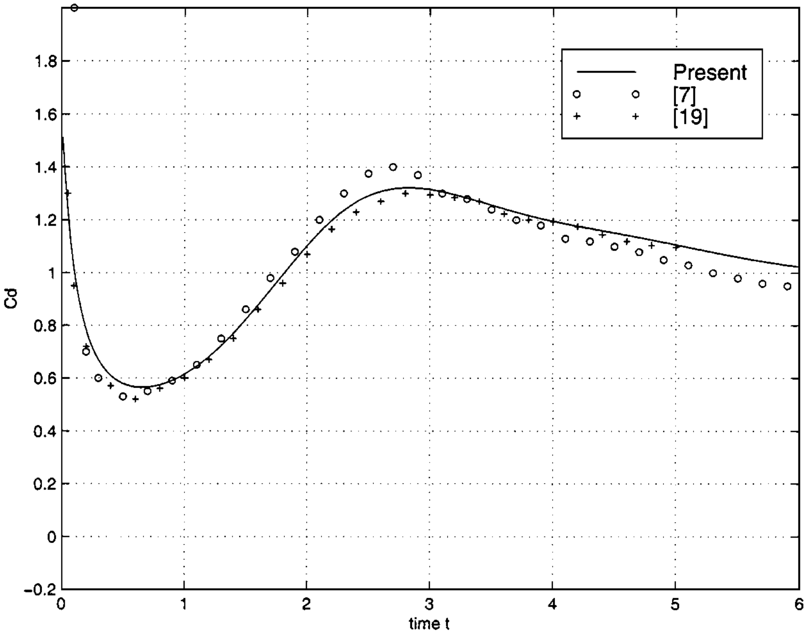

FIG. 15. Comparison of drag coefficients, $Re = 1000$.

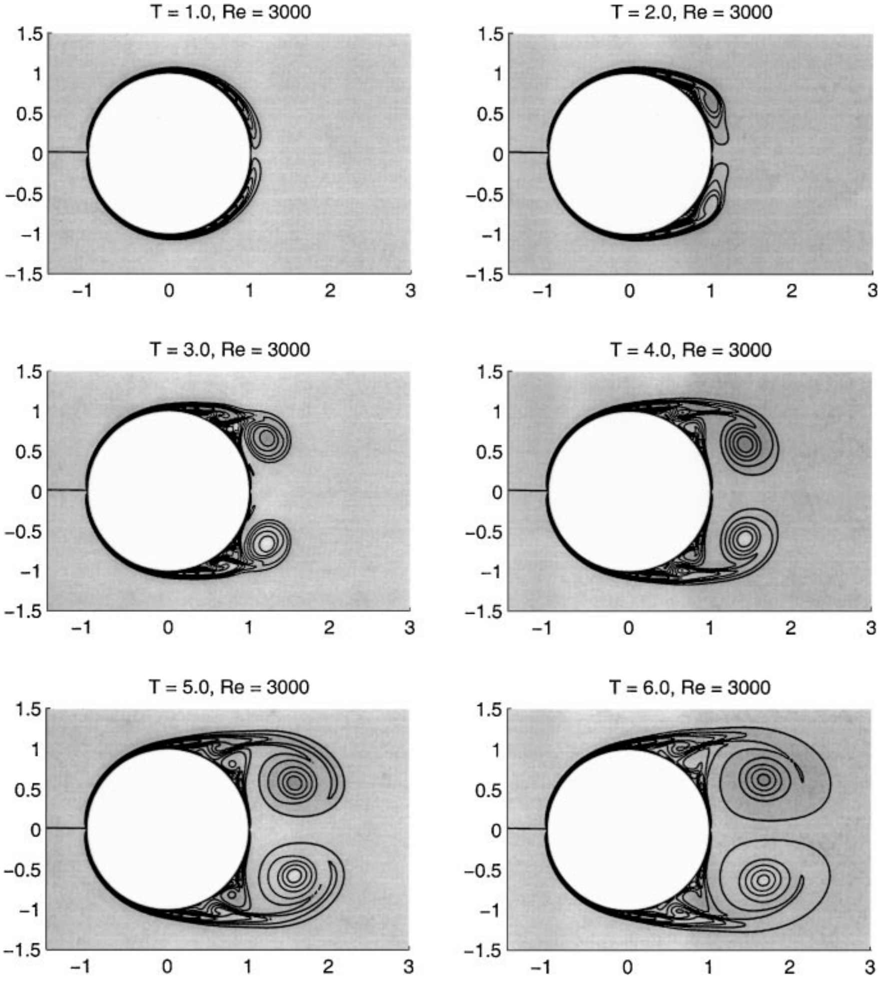

FIG. 16. Vorticity contours: $Re = 3000$.

is around 13,000, while for the same time T, 300,000 vortex elements have been used in their study. The result from Cheng *et al.* [7] by using a hybrid vortex method is also presented in Fig. 18 which, due to the relatively low resolution and the additional numerical diffusion, does not exhibit capture of the drag plateau. In Fig. 18, the C_d result from a higher grid resolution (320×300) with $\Delta Y_1 = 0.005$ is also presented, which shows that better agreement with the result from Shankar has been achieved by refining the grids.

In Fig. 19, the streamlines for time $T = 5.0$ are presented, which compare well with the experimental flow visualisation of Bouard and Coutanceau [5].

In Fig. 20, the radial velocity distributions along the rear centre line of the circular cylinder are compared with the result from [29] for $T = 1.0, 2.0, 3.0, 4.0$, and 5.0, and again excellent agreement has been achieved.

Re = 9500. This case is the highest *Re* for which simulations are performed in the present study and is by far the most interesting and challenging one [19]. For the results

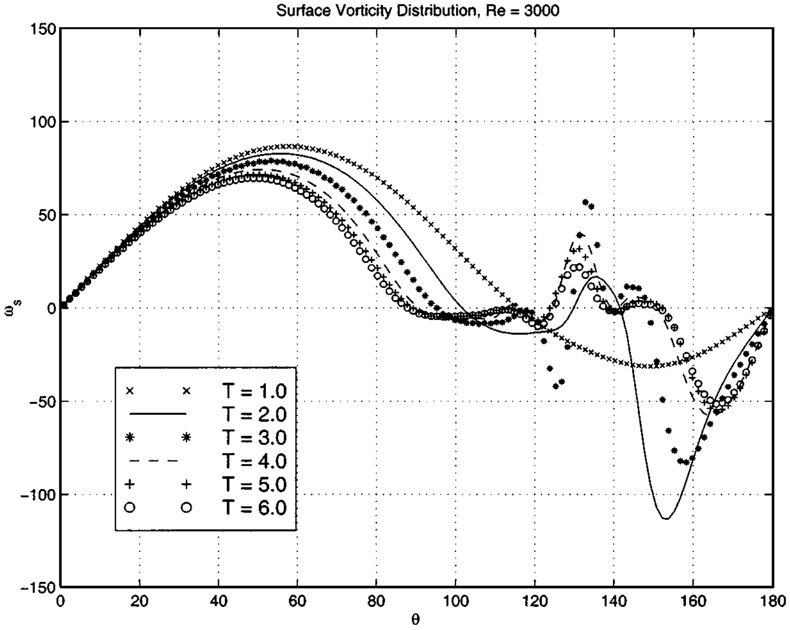

FIG. 17. Surface vorticity distribution: $Re = 3000$.

presented , 640 × 280 grid points have been used with a minimum grid size in the normal direction to the surface $\Delta Y_1 = 0.005$ and the time step $\Delta t = 0.002$. Figures 21 and 22 show the vorticity distribution at the body surface and the equi-vorticity contours for $T = 1.0$, 2.0, and 3.0, respectively. In Fig. 23, the C_d values are compared with those presented by Shankar

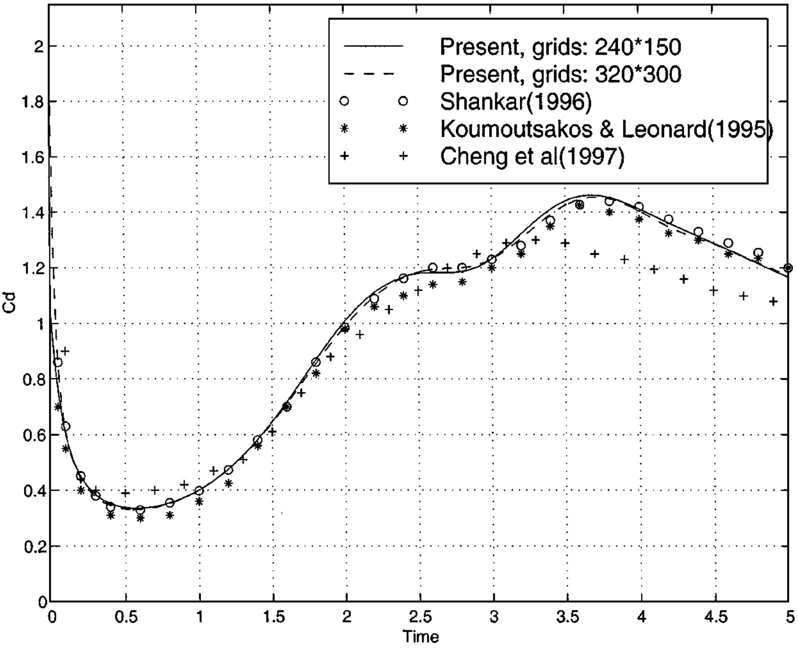

FIG. 18. Comparison of drag coefficients, $Re = 3000$.

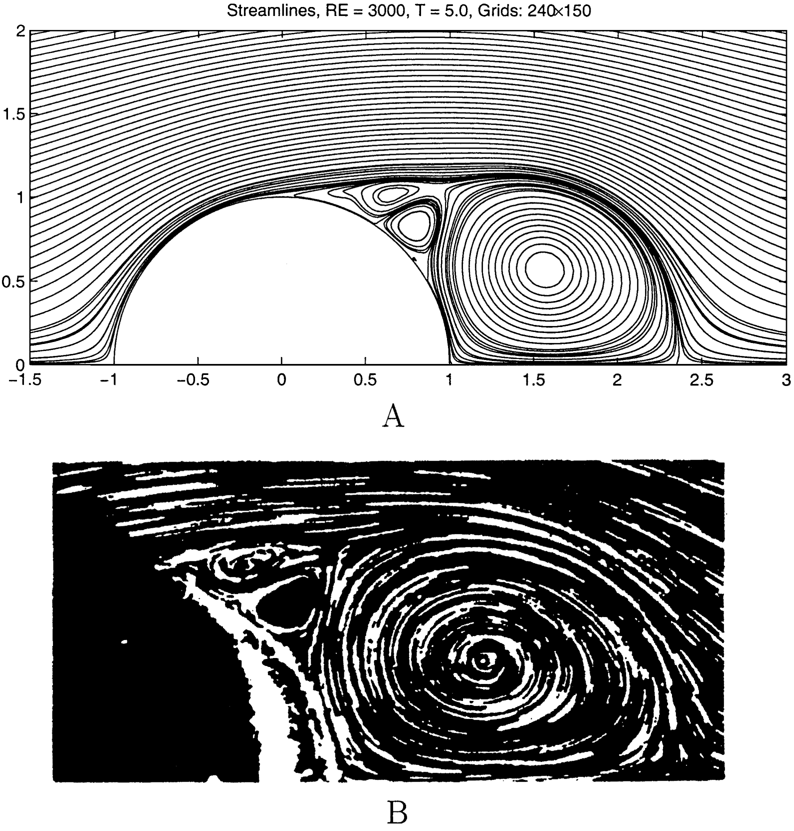

FIG. 19. Streamlines for *Re* = 3000: (A) Calculated, (B) Experiments [5].

and Van Dommelen [29] and Kruse and Fischer [20], which show a very good agreement among the results from different methods. for the present study, by the end of the calculation ($T = 3.0$), the number of active cells is around 33,000, while for the same time T, 350,000 vortex elements have been used in the study by Koumoutsakos and Leonard [19] and 2044 × 254 grid points was used by Anderson and Reider [1]. In the Kruse and Fischer's work, a spectral elements method has been used to solve the Navier–Stokes equations in terms of velocity and pressure. The computational grids consist of 6112 spectral element and there are 10 nodes along each dimension in every element. Although a similar number of vortex elements were employed in the Shankar's work in which, by the end of time $T = 3.0$, 60,000 vortices are required, a far more expensive procedure was adopted therein for calculating the viscous diffusion.

In Fig. 24, the radial velocity distributions along the rear centre line of the circular cylinder are also compared with the result from Shankar for $T = 1.0$, 2.0, 3.0.

4.4. *Long Time Calculation: Re* = 1000

In this section, the long time evolution of the flow around an impulsively started cylinder at $Re = 1000$ is presented. The grid points used for the simulation are $NI \times NJ = 160 \times 220$

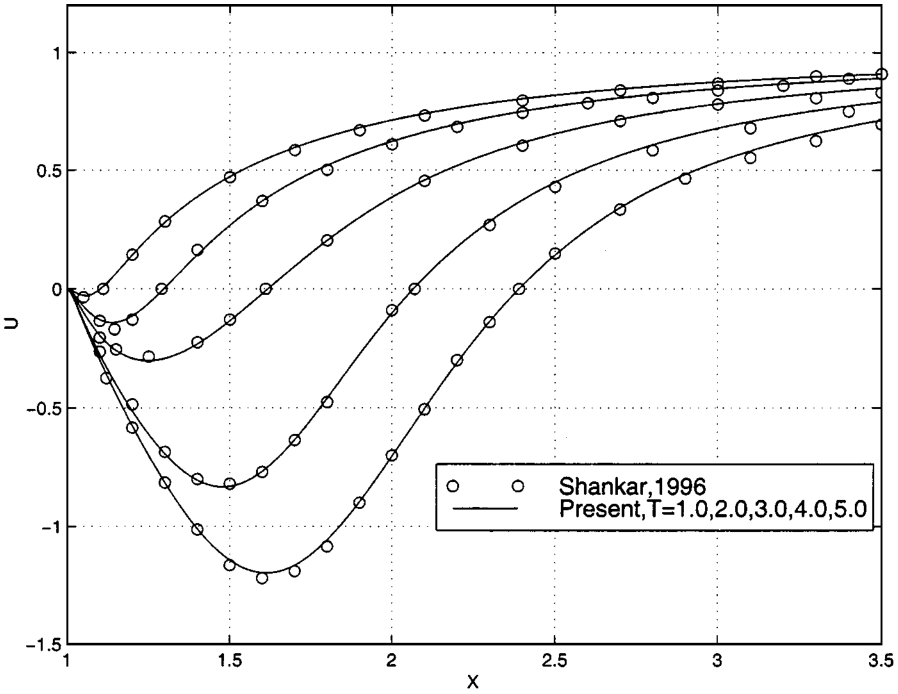

FIG. 20. Radial velocity distribution along the rear centre line of the circular cylinder, $Re = 3000$.

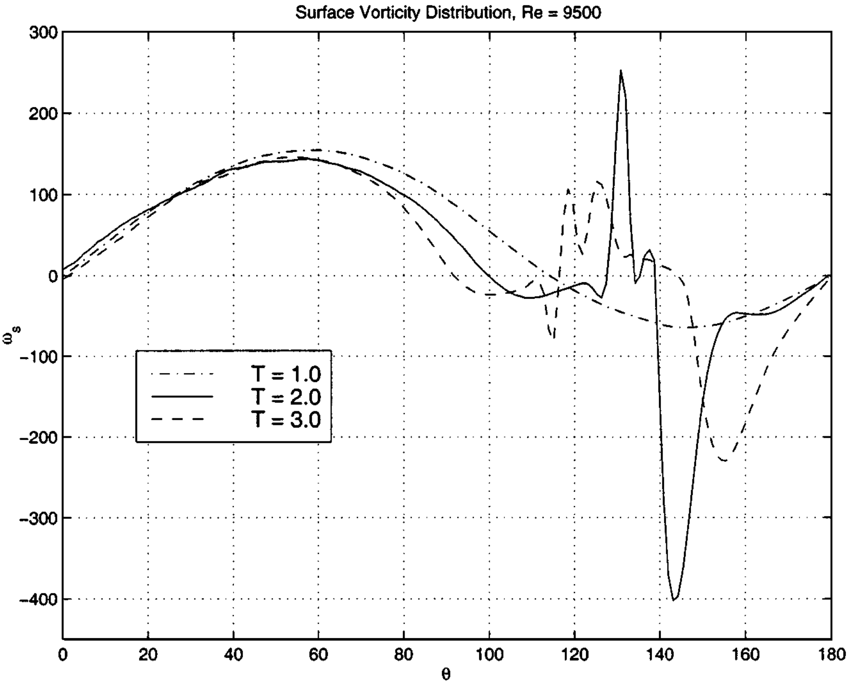

FIG. 21. Surface vorticity distribution: $Re = 9500$.

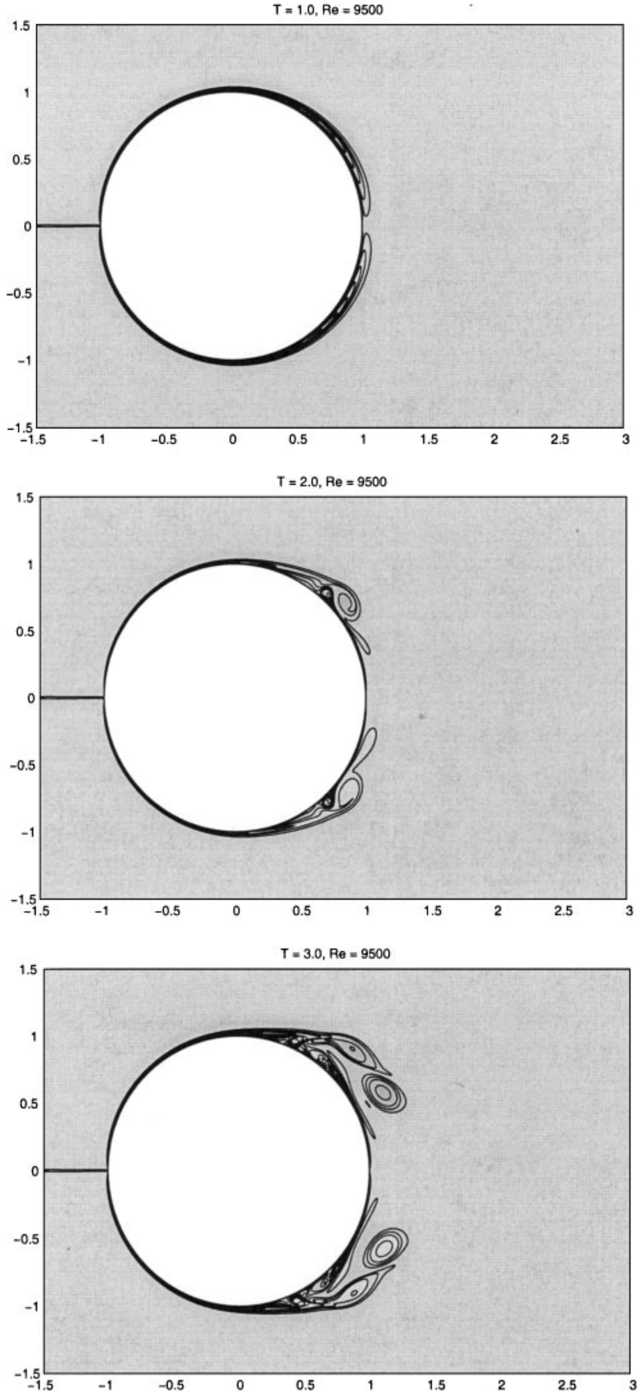

FIG. 22. Vorticity contours: $Re = 9500$.

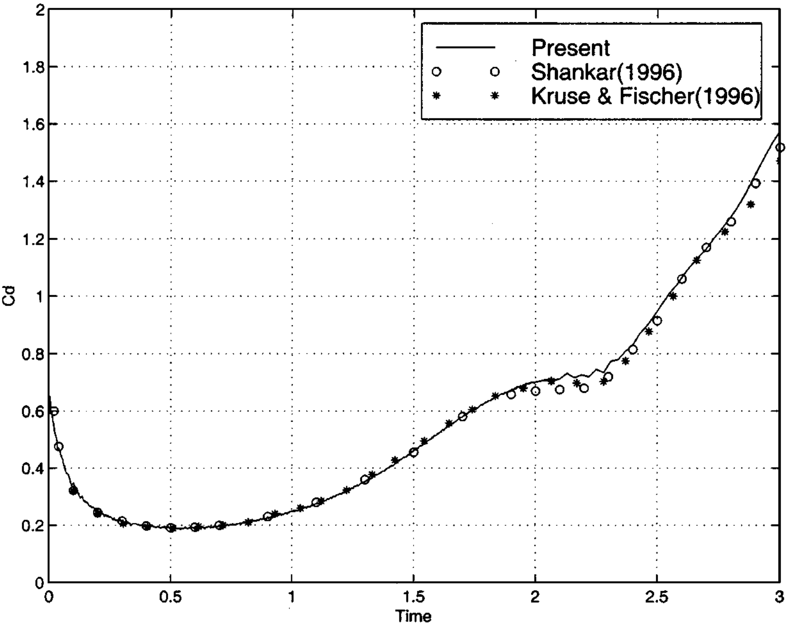

FIG. 23. Comparison of drag coefficients, $Re = 9500$.

with $\Delta Y_1 = 0.02$ and the time step is $\Delta t = 0.01$. Figure 25 gives two snapshots of the flow in terms of vorticity contours, which show vortices alternately shedding from the rear part of the cylinder. In Fig. 26, the corresponding streamlines for $T = 168$ are also given. The evolution of the drag and lift coefficients is presented in Fig. 27. In the present study,

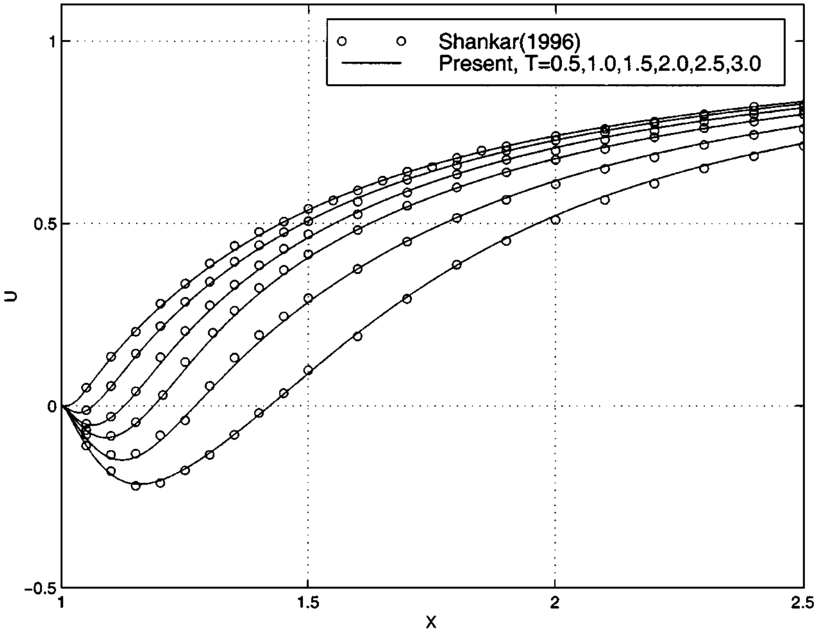

FIG. 24. Radial velocity distribution along the rear centre line of the circular cylinder, $Re = 9500$.

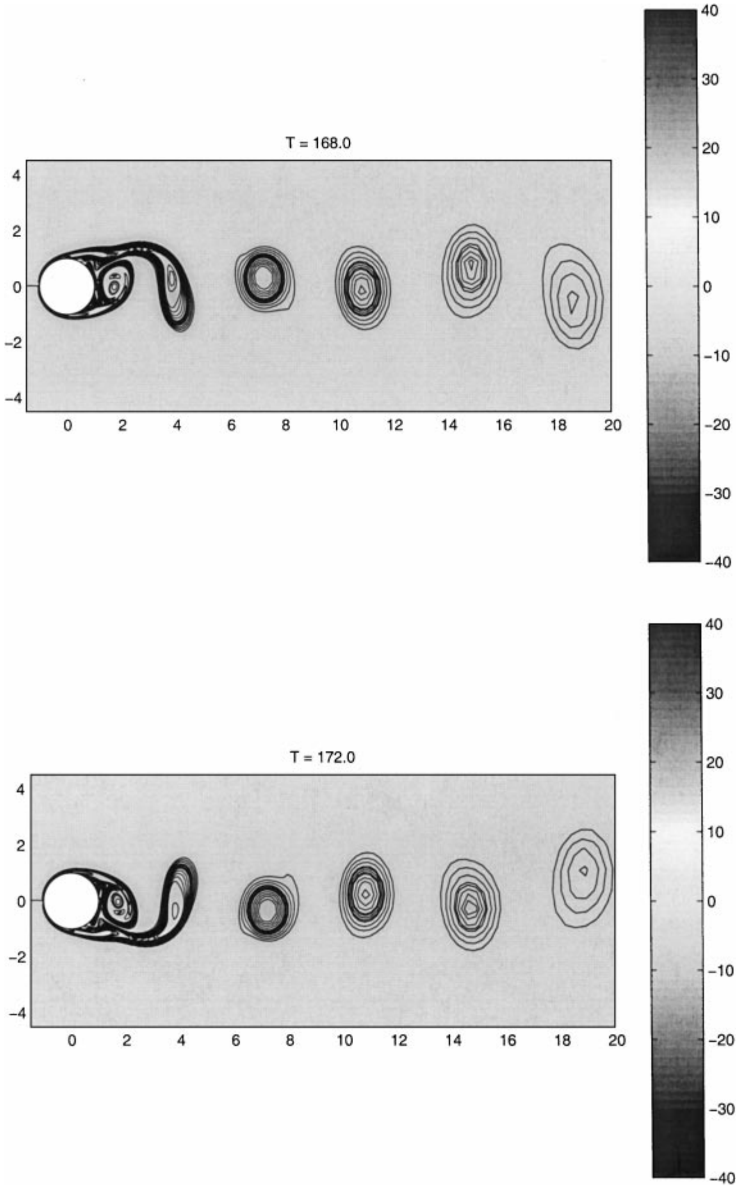

FIG. 25. Vorticity contours for $Re = 1000$: long time calculation.

no artificial perturbation was applied to the flow to initiate the alternate vortex shedding; instead, it is triggered solely by the numerical errors (truncation and roundoff errors) during the calculation. After a long time evolution, say $T > 100$, the vortex shedding process finally settles down, forming the regular vortex pattern in the wake. From Fig. 27, it can be calculated that the average C_d value after $T > 120$ is about 1.52 and the Strouhal number St is about 0.24. Both results are in good agreement with other numerical results from 2-D simulations, as shown in Table I, where the experimental result from Roshko [27] is also presented.

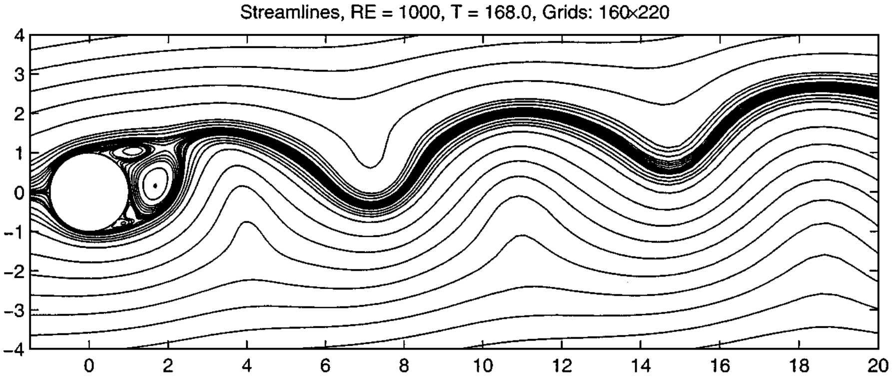

FIG. 26. Streamlines for $Re = 1000$, $T = 168.0$.

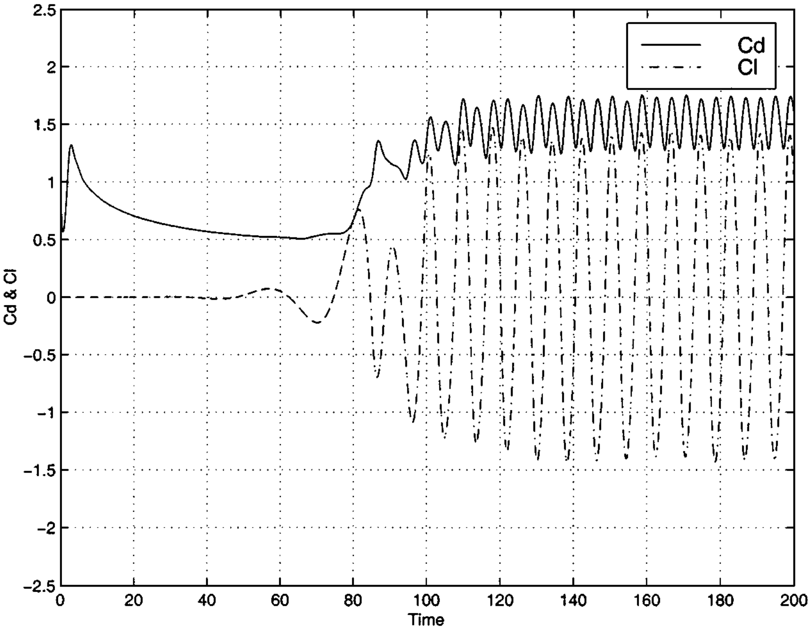

FIG. 27. Evolution of drag and lift coefficients.

TABLE I

Drag coefficient and Strouhal number for *Re* = 1000

	Behr *et al.*	Blackburn *et al.*	Cheng *et al.*	Mittal *et al.*	Roshko	Present
C_d	1.53	1.51	1.23	1.53	1.20	1.52
S_t	0.241	–	0.206	0.245	0.21	0.240

5. CONCLUSIONS

A new method based on the vorticity formulation has been presented in this paper for unsteady incompressible viscous flow problems. By solving the vorticity transport equation using the finite-volume method and calculating velocity using a modified Biot–Savart law, only the flow field region with non-zero vorticity needs to be solved. High efficiency has been achieved by employing an adaptive fast summation algorithm for the velocity calculations. During the calculation, mass and vorticity conservation can be guaranteed by using this approach together with the method of implementing the surface boundary conditions. The accuracy and efficiency of the method have been demonstrated by studying both the early stage development and long term evolution of the flow around an impulsively started circular cylinder at various *Re* number regimes and by comparing present results with other numerical and experimental results. Particularly, for high *Re* number simulations, a highly accurate solution has been obtained without using excessively large numbers of grid points which are needed by most other methods.

The method is currently being combined with the discrete vortex method in a domain decomposition approach and is also being extended to 3-D flow problems.

ACKNOWLEDGMENTS

The authors thank the referees for their helpful comments on the paper.

REFERENCES

1. C. R. Anderson and Marc B. Reider, A high order explicit method for the computation of flow about a circular cylinder, *J. Comput. Phys*. **125**, 207 (1996).
2. G. R. Batchelor, *An Introduction to Fluid Dynamics* (Cambridge Univ. Press, Cambridge, UK, 1967).
3. M. Behr, J. Liou, R. Shih, and T. E. Tezduyar, Vorticity-stream function formulation of unsteady incompressible flow around a cylinder: Sensitivity of the computed flow field to the location of the out flow boundary, *Int. J. Numer. Meth. Fluid* 323 (1991).
4. H. M. Blackburn and R. D. Henderson, A study of two-dimensional flow past an oscillating cylinder, *J. Fluid Mech*. **385**, 255 (1999).
5. R. Bouard and M. Coutancea, The early stage development of the wake behind an impulsively started cylinder for $40 < Re < 10^4$, *J. Fluid Mech*. **101**, 587 (1980).
6. C. C. Chang and R. L. Chern, A numerical study of flow around an impulsively started circular-cylinder by a deterministic vortex method, *J. Fluid Mech*. **233**, 243 (1991).
7. M. Cheng, T. Chew, and S. C. Luo, A hybrid vortex method for flows over a bluff body, *Int. J. Numer. Meth. Fluids* **24**, 253 (1997).
8. A. J. Chorin, Numerical study of slightly viscous flow, *J. Fluid Mech.* **57**, 785 (1973).
9. M. H. Chou, Simulation of slight viscous external flow by a grid-particle domain decomposition method, *Comput. Fluids* **24**, 333 (1995).
10. J. P. Christansen, Numerical simulation of the hydromechanics by the method of point vortices, *J. Comput. Phys.* **13**, 369 (1973).
11. N. R. Clarke and O. R. Tutty, Construction and validation of a discrete vortex method for two-dimensional incompressible Navier–Stokes equations, *Comput. Fluids* **23**, 751 (1994).
12. L. Van Dommelen and E. A. Rundensteiner, Fast, adaptive summation of point forces in the two-dimensional poisson equation, *J. Comput. Phys.* **83**, 126 (1989).
13. J. H. Ferziger and M. Peric, *Computational Methods for Fluid Dynamics* (Springer-Verlag, Berlin, 1996).

14. A. Gharakhani and A. F. Ghoniem, Three-dimensional vortex simulation of the time-dependent incompressible internal viscous flows, *J. Comput. Phys.* **134**, 75 (1997).
15. L. Greengard and V. Rokhlin, A fast algorithm for particle simulations, *J. Comput. Phys.* **73**, 325 (1987).
16. L. Greengard and W. D. Gropp, A parallel version of the fast multipole method, *Comput. Math. Appl.* **20**, 63 (1990).
17. P. M. Gresho, Imcompressible fluid dynamics: some fundamental formulation issue, *Ann. Rev. Fluid Mech.* **23**, 413 (1991).
18. H. Lamb, Hydrodynamics, 6th ed. (Cambridge Univ. Press, Cambridge, UK, 1932).
19. P. Koumoutsakos and A. Leonard, High-resolution simulations of the flow around an impulsively started cylinder using vortex methods, *J. Fluid Mech.* **296**, 1 (1995).
20. G. W. Kruse and P. Fischer, *Center for Fluid Mechanics* (Brown University, 1996).
21. A. Leonard, Vortex methods for flow simulation, *J. Comput. Phys.* **37**, 289 (1980).
22. A. Leonard, Computing three-dimensional incompressible flows with vortex elements, *Ann. Rev. Fluid Mech.* **17**, 523 (1985).
23. A. Leonard, Direct numerical simulation, *in Simulation and Modeling of Turbulent Flows*, edited by T. B. Gatski and M. Y. Hussaini (Oxford Univ. Press, London, 1996).
24. H. Q. Lin, M. Vezza and R. A. McD. Galbrath, Discrete vortex method for simulating unsteady flow around pitching aerofoils, *AIAA J.* **35**, 494 (1997).
25. S. Mittal, *Stabilized Space–time Finite Element Formulation for Unsteady Incompressible Flows*, Ph.D. thesis, (University of Minnesota, 1992).
26. L. Qian and M. Vezza, *The 3-D Vortex Particle Method and the Fast Summation Algorithm*, Glasgow University Aero Report No. 9620 (1996).
27. A. Roshko, *On the Development of Turbulent Wakes from Vortex Sheets*, NACA Report 1191 (1954).
28. T. Sarpkaya, Computational methods with vortices—The 1988 Freeman scholar lecture, *J. Fluid Eng.* **111**, 5 (1989).
29. S. Shankar and L. Van Dommelen, A new diffusion procedure for vortex methods, *J. Comput. Phys.* **127**, 88 (1996).
30. S. Shankar, *A New Mesh-free Vortex Method*, Ph.D thesis, (Florida State University, 1996)
31. W. Z. Shen, and T. P. Loc, A coupling finite difference particle method for the resolution 2D navier–stokes equations in velocity–vorticity form, *Aerospace Sci. Tech.* **1**, 97 (1997).
32. P. R. Spalart, *Vortex Methods for Separated Flows*, NASA TM 100068 (1988).
33. I. H. Tuncer, J. C. Wu, and C. M. Wang, Theoretical and numerical studies of oscillating airfoils, *AIAA J.* **28**, 1614 (1990).
34. G. S. Winckelmans and A Leonard, Contribution to vortex particle methods for the computation of three-dimensional incompressible unsteady flows, *J. Comput. Phys.* **109**, 247 (1993).
35. J. C. Wu and U. Gulcat, Separate treatment of attached and detached flow regions in general viscous flows, *AIAA J.* **19**, 20 (1981).
36. J. C. Wu and J. F. Thompson, Numerical solution of time-dependent imcompressible Navier–Stokes equation using an integro-differential formulation, *Comput. Fluids* **1**, 197 (1973).